IEEE Open Journal of
Industry Applications

Received 12 June 2023; revised 21 August 2023 and 14 September 2023; accepted 3 October 2023. Date of publication 11 October 2023; date of current version 9 November 2023. The review of this article was arranged by Associate Editor H. W. Kim.

Digital Object Identifier 10.1109/OJIA.2023.3323855

Operation, Design, and Losses of the Modular Multilevel Matrix Converter in a Flywheel Energy Storage System

JONAS KIENAST [1], STEFFEN BERNET [1] (Senior Member, IEEE), AND GINO STURM [2]

[1]Chair of Power Electronics, TU-Dresden, 01069 Dresden, Germany
[2]Chair of Electrical Machines and Drives, TU-Dresden, 01069 Dresden, Germany

CORRESPONDING AUTHOR: JONAS KIENAST (e-mail: jonas.kienast@tu-dresden.de)

This work was supported by the Federal Ministry for Economic Affairs and Climate Action on the basis of a decision by the German Bundestag under Grant 03EI6061D.

ABSTRACT This article presents an analysis of selected characteristics of the modular multilevel matrix converter (M3C) operating a doubly fed induction generator (DFIG) in a flywheel energy storage system. A detailed analysis of the necessary electrical input and output quantities, as well as the identification of required internal currents and voltages, leads to a newly introduced iterative design process for the converter. This process ultimately provides information on the required number of submodules and demonstrates the overload capability of the converter in reactive power operation. Also, the short-circuit current contribution of the system for this unique configuration of M3C and DFIG is investigated for the first time. Taking into account the unique operating characteristics of the M3C, a loss analysis of the converter and the machine is performed, and a loss-optimized distribution of reactive power between the machine and the converter is proposed. The article is conducted analytically and is validated by experimental results on a small-scale demonstrator.

INDEX TERMS Doubly fed induction generator (DFIG), flywheel energy storage system (FESS), loss calculation, modular multilevel matrix converter (M3C).

I. INTRODUCTION

The shift toward renewable energy sources, like wind and photovoltaic, is inevitable to reduce CO_2 emissions. However, the integration of these renewable energy sources into power grids creates new challenges regarding grid stability. The number of synchronous generators (SGs) providing the grid frequency stabilizing inertial response and voltage stabilizing reactive power will decrease as conventional energy sources based on, e.g., coal or natural gas, are phased out. Therefore, new solutions for grid voltage and frequency stabilizations have to be explored, developed, and implemented [1]. The authors of [2] show that the modular multilevel matrix converter (M3C) can play a significant role in addressing some of these challenges. A high-power flywheel energy storage system (FESS) (see Fig. 1) is able to stabilize large grid areas. It consists of a large flywheel, a high-power doubly fed induction generator (DFIG), and an M3C. By accelerating or decelerating the flywheel, the system can emulate the inertial response of SG in case of grid frequency deviations [3]. Also, additional frequency stabilizing measures, such as a fast frequency response, can be implemented [2]. Furthermore, the supply and control of reactive power enable grid voltage control. In order to stabilize large grid

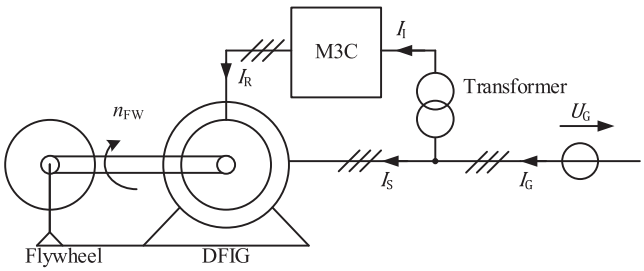

FIGURE 1. Single line diagram of the high-power flywheel energy storage system (FESS).

areas, a high-power rating of the system in the range of a few 100 MVA is necessary. Comparable DFIGs in pump storage plants are frequently operated by cycloconverters [4]. However, line commutated converters do not offer an interdependent control of active and reactive power, which is necessary for grid supporting energy storage systems. Furthermore, line commutated converters require large and expensive filters in order to comply with grid standards [4]. In contrast, the M3C offers fast and independent control of real and reactive power, and it is able to support the grid in symmetrical and asymmetrical failure cases. The M3C is especially suited for high-power applications (e.g., several 10 MVA–several 100 MVA), while the multilevel output voltage enables a design with very small grid filters. Furthermore, the redundancy on submodule level results in a high availability of the converter. Compared to the modular multilevel converter (M2C), the circulating currents and the expense of submodule capacitors are reduced at low output frequencies (e.g., 0 Hz–10 Hz), which are typical for the rotor circuit of the DFIG [2], [5].

This article presents a detailed analysis of the operation and design of the M3C in a high-power FESS. The M3C operating regime is investigated and a new iterative converter design process is derived. Also, the capability to support the grid in severe voltage dips is investigated analytically.

Assuming an operation period of more than 20 years, a reduction of losses in the FESS enables significant cost savings. An advantageous distribution of reactive power between the DFIG stator and the M3C input side is a degree of freedom to reduce losses. So far, several research groups investigated the reactive power distribution in wind energy conversion systems with DFIGs. However, only two-level voltage source converters (2L-VSC) in back-to-back configuration were considered [6], [7]. Therefore, this article aims to provide analytical loss calculations of M3C and DFIG to derive a loss-optimal distribution of reactive power considering the unique operating characteristics of the M3C. The analytical findings are verified on a scaled 8 kVA demonstrator of the FESS. The rest of the article is organized as follows. Section II gives an overview about the operation of the energy storage at the PCC, and defines the operating area of DFIG and M3C. Furthermore, a new iterative design process for the M3C is presented. Based on the operating regimes of the machine and the converter, a model for the corresponding losses is derived in Section III. Section IV describes a new operation method, which reduces losses by the useful distribution of reactive power to converter and stator of the DFIG. Section V presents experimental results confirming the analytical model and operation method. Finally, Section VI concludes this article.

II. OPERATION OF THE FESS

This section defines the operating area of the FESS. After giving the analytical fundamentals of the DFIG and M3C, some unique operational characteristics of the M3C in combination with a DFIG are introduced for the first time, concerning the balancing and short-circuit current contribution of the system.

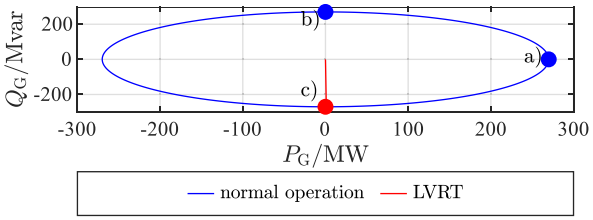

FIGURE 2. Safe operating area of the FESS for normal operation and in LVRT scenarios. Bullet points show the operating points relevant for Fig. 4.

The analytical calculations are used in Section III in order to calculate the losses of the system.

A. BEHAVIOR AT THE POINT OF COMMON COUPLING

In order to stabilize the grid frequency f_G, the FESS operation is similar to the behavior of an SG regarding synthetic inertia and grid voltage stabilization [3]. Therefore, the active power output is adjusted proportionally to the rate of change of frequency. For larger frequency deviations, a fast frequency response mode is implemented, where the active power output is proportional to the total frequency deviation [2]. An inductive or capacitive behavior of the FESS reduces or increases the grid voltage. Thus, the grid voltage is stabilized by providing reactive power proportional to the grid voltage deviation. In case of a grid voltage dip, the FESS should stay connected to the grid and supply a reactive current [low voltage ride through (LVRT) behavior]. For this article, a symmetrical three-phase voltage dip to 10% of the rated grid voltage $U_{G,r}$ is considered. Fig. 2 shows the safe operating area of the FESS assuming a speed range of the flywheel between 1200 rpm and 1800 rpm.

B. OPERATION OF THE DOUBLY FED INDUCTION GENERATOR

1) MODEL

The mathematical model of the DFIG is given in (1)–(4). The subscript S/R refers to the stator/rotor quantities.

The superscripted S/R gives indication that the coordinate system refers to the stator/rotor. The magnetizing inductance is represented by L_M. The rotor quantities are referred to the stator voltage using the transfer ratio k_{DFIG} of the DFIG

$$\underline{U}_S^S = R_S \cdot \underline{I}_S^S + \frac{d\underline{\Psi}_S^S}{dt} \tag{1}$$

$$\underline{U}_R^R = R_R \cdot \underline{I}_R^R + \frac{d\underline{\Psi}_R^R}{dt} \tag{2}$$

$$\underline{\Psi}_S^S = L_S \cdot \underline{I}_S^S + L_M \cdot \underline{I}_R^S \tag{3}$$

$$\underline{\Psi}_R^R = L_R \cdot \underline{I}_R^R + L_M \cdot \underline{I}_S^R. \tag{4}$$

Considering the speed of the flywheel n_{FW} and the number of pole pairs of the machine p the slip s of the machine can be

derived using

$$s = \frac{f_G - n_{FW} \cdot p}{f_G}. \tag{5}$$

The active power in the stator P_S and rotor P_R determine the active power in the grid

$$P_G = P_R + P_S \cong P_S \cdot (1 - s) \tag{6}$$

if the losses of the M3C and transformer are neglected [5].

The reactive power in the grid

$$Q_G = \underbrace{Q_{I,M3C} + Q_T}_{Q_{PT}} + Q_S \tag{7}$$

is the sum of the reactive powers of the stator Q_S, the grid side of the M3C $Q_{I,M3C}$, and the reactive power demand of the transformer Q_T. This reactive power demand arises from the inductive voltage drop across the windings of the transformer. The required reactive grid power can be distributed freely between the stator of the machine and the converter input. This is defined by the factor

$$\alpha = \frac{Q_S}{Q_G}. \tag{8}$$

By adjusting α, depending on the operating point, the losses of the system can be reduced (see Section IV). The M3C has to compensate the inductive reactive power of the transformer Q_T in order to match the reactive power demand at the primary side of the transformer Q_{PT}.

2) OPERATION

During normal operation of the DFIG, the rotor quantities of the positive sequence (superscripted 1) have a smaller frequency

$$f_R^1 = s \cdot f_G \tag{9}$$

than the stator quantities, depending on the slip of the machine. The magnitude of the voltages and currents are calculated using (1)–(4), while considering a stator current calculated by

$$\underline{I}_S^{*S} = \frac{P_S + j \cdot Q_S}{3 \cdot \underline{U}_S^S}. \tag{10}$$

The authors in [8] and [9] present an analytical description of the DFIG during voltage dips, utilizing (1)–(4). Voltage dips generate a dc-component $\underline{\Psi}_S^{S,N}$ in the stator flux linkage to maintain continuity in the flux linkage. As the machine's rotor continues to rotate, this natural flux induces high voltages in the rotor with the frequency

$$f_R^N = (1 - s) \cdot f_G. \tag{11}$$

To demagnetize the natural component, an appropriate dc current $\underline{I}_S^N$ is utilized in the stator. Therefore, the stator current consists of the positive sequence current $\underline{I}_S^{S,1}$ and the natural stator current $\underline{I}_S^N$ as expressed in

$$\begin{aligned} \underline{I}_S^S &= \underline{I}_S^{S,1} + \underline{I}_S^{S,N} \\ &= \hat{I}_S^1 \cdot e^{j \cdot (\omega_G \cdot t - \varphi_1)} + \hat{I}_S^N \cdot e^{-j\varphi_N}. \end{aligned} \tag{12}$$

The positive sequence current is reliant on the demanded short-circuit power

$$S_{SC} = \sqrt{3} \cdot U_{G,r} \cdot I_S^{S,1}. \tag{13}$$

The amplitude of the natural current is selected to ensure that the maximum rotor voltage does not surpass the maximum rotor insulation voltage $U_{R,max}$, but should be as minimum as possible, as the short-circuit current contribution is reduced by a high natural current component (see Section II-C2).

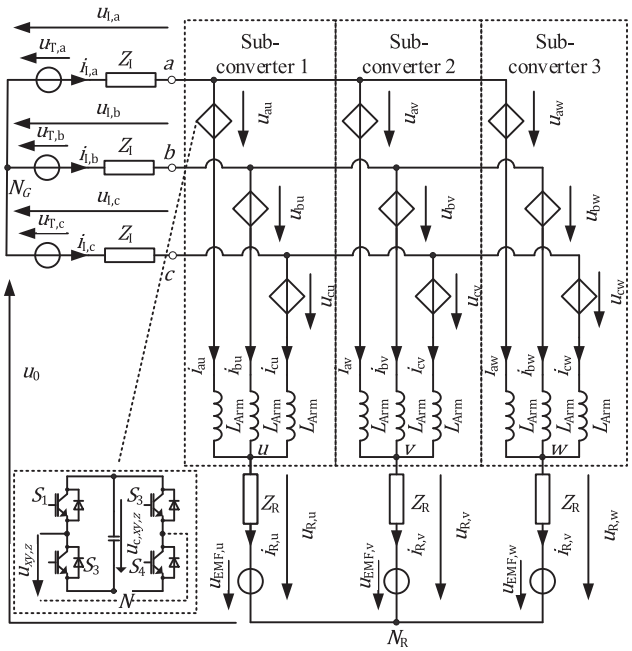

FIGURE 3. Modular multilevel matrix converter with controlled voltage sources representing the series connection of N_S full bridges.

C. MODEL AND OPERATION OF THE M3C

1) MODEL

The M3C performs a direct AC to AC conversion and comprises of three subconverters, each containing $3 \cdot N_P$ arms, where N_P is the number of parallel arms in order to increase the arm current rating. It is depicted in Fig. 3 for $N_P = 1$. The arms consist of N_S full-bridge submodules connected in series with the arm inductor L_{Arm}. The M3C's input is connected to the secondary side of the transformer.

The secondary voltage of the transformer $u_{T,x} = u_{S,x} \cdot k_T$, where $x \in [a, b, c]$ is derived using the transformers transfer ratio k_T. The input current $i_{I,x}$ flows through the input impedance Z_I which mainly includes the transformer's stray inductances. The M3C's input voltage $u_{I,x}$ is the sum of the

grid voltage and the voltage drop across the input impedance. The output terminals are connected to the DFIG rotor, with the back EMF represented by a voltage source $u_{\mathrm{EMF},y}$, where $y \in [\mathrm{u}, \mathrm{v}, \mathrm{w}]$. The M3C's output voltage $u_{\mathrm{R},y}$ is the sum of the back EMF and the voltage drop across the rotor impedance Z_{R}, which is dependent on the rotor current $i_{\mathrm{R},y}$. Each full-bridge module generates three voltage levels in the output voltage $u_{xy,z}$ with $z \in [1 : N_{\mathrm{S}}]$, by switching the positive or negative capacitor voltage $u_{\mathrm{C},xy,z}$ to the output terminals, or bypassing the capacitor to create a third voltage level. The arm voltage

$$u_{xy} = \sum_{z=1}^{N_{\mathrm{S}}} u_{xy,z} \tag{14}$$

is the sum of the output voltages produced by each full bridge, while the arm capacitor voltage

$$u_{\mathrm{C},xy} = \sum_{z=1}^{N_{\mathrm{S}}} u_{\mathrm{C},xy,z} \tag{15}$$

is the sum of each cell's capacitor voltage. The common mode voltage between the grid's star points N_{G} and the rotor's N_{R} is denoted as u_0. The arm currents

$$i_{\mathrm{au}} = \frac{i_{\mathrm{I},\alpha}}{3 \cdot N_{\mathrm{P}}} + \frac{i_{\mathrm{R},\alpha}}{3 \cdot N_{\mathrm{P}}} + i_{\mathrm{D1},\alpha} + i_{\mathrm{D2},\alpha} \tag{16}$$

are composed of the input and rotor currents as well as the diagonal currents i_{D1} and i_{D2}, which circulate inside the converter and can be used for balancing [10]. The input current

$$I_{\mathrm{I}}^{*} = \frac{P_{\mathrm{I,M3C}} + j \cdot Q_{\mathrm{I,M3C}}}{3 \cdot k_{\mathrm{T}} \cdot \underline{U}_{\mathrm{S}}^{\mathrm{S}}} \tag{17}$$

depends on the active power $P_{\mathrm{I,M3C}}$ and reactive power at the input of the M3C. The arm voltage is calculated similar to the arm currents as shown in (18) [10]. However, it can be stated that in steady-state operation the diagonal voltages and the common mode voltage are small in contrast to the voltages at the rotor and the input side [10]

$$u_{\mathrm{au}} = u_{\mathrm{I},\alpha} - u_{\mathrm{R},\alpha} + u_{\mathrm{D1},\alpha} + u_{\mathrm{D2},\alpha} + u_0 \approx u_{\mathrm{I},\alpha} - u_{\mathrm{R},\alpha}. \tag{18}$$

Using (16) and (18), the arm power

$$p_{xy} = u_{xy} \cdot i_{xy} \tag{19}$$

is derived. When using a suitable modulation technique [11], the arm energy

$$w_{xy} = \int_0^{t'} p_{xy} \mathrm{d}t \tag{20}$$

is distributed equally over all capacitors within one arm. Therefore, the capacitor voltage

$$u_{\mathrm{C},xy,z} = \sqrt{\frac{2 \cdot w_{xy}}{N_{\mathrm{S}} \cdot C_{\mathrm{SM}}}} = \bar{u}_{\mathrm{C},xy,z} + \tilde{u}_{\mathrm{C},xy,z} \tag{21}$$

is dependent on the number of submodules and the submodule capacity C_{SM}. It consists a dc part $\bar{u}_{\mathrm{C},xy,z}$ and an alternating component $\tilde{u}_{\mathrm{C},xy,z}$.

2) OPERATION

During normal operation, the output frequencies of the rotor voltage and rotor current are small in magnitude [see (9)] when the machine is operated within a reasonable slip range (e.g., $s \epsilon [-0.2; 0.2]$). In case of an LVRT, a frequency close to the grid frequency [see (11)] appears in the rotor components. It can be taken from [10] that an operation of the M3C at low output frequencies or with similar input and output frequencies leads to a high capacitor voltage ripple. To avoid excessively large submodule capacitors, additional diagonal currents and common mode voltages are applied. On the other hand, the diagonal currents influence the required power semiconductor current rating and the converter losses. The required diagonal current amplitudes for low-frequency operation is shown as

$$\hat{I}_{\mathrm{D1}} = \begin{cases} \frac{1}{3} \cdot \frac{\hat{U}_{\mathrm{R}}^{1}}{\hat{U}_{\mathrm{E}}^{1}} \cdot \frac{\hat{I}_{\mathrm{R}}^{1}}{N_{\mathrm{P}}} \text{ for } 0 < s < 0.2 \\ 0 \text{ for } s \leq 0 \end{cases} \tag{22}$$

$$\hat{I}_{\mathrm{D2}} = \begin{cases} \frac{1}{3} \cdot \frac{\hat{U}_{\mathrm{R}}^{1}}{\hat{U}_{\mathrm{E}}^{1}} \cdot \frac{\hat{I}_{\mathrm{R}}^{1}}{N_{\mathrm{P}}} \text{ for } -0.2 < s \leq 0 \\ 0 \text{ for } s > 0. \end{cases} \tag{23}$$

The necessary compensation measures for similar input and output frequencies, as it is the case during a LVRT [see (11)], involve the use of two parts of the diagonal current $I_{\mathrm{D},2}$ where the amplitudes are

$$\hat{I}_{\mathrm{D2},1} = -\frac{1}{3} \cdot \frac{\hat{U}_{\mathrm{R}}^{\mathrm{N}}}{\hat{U}_0} \cdot \frac{\hat{I}_{\mathrm{I}}}{N_{\mathrm{P}}} \tag{24}$$

$$\hat{I}_{\mathrm{D2},2} = \frac{1}{3} \cdot \frac{\hat{U}_{\mathrm{I}}}{\hat{U}_0} \cdot \frac{\hat{I}_{\mathrm{R}}^{\mathrm{N}}}{N_{\mathrm{P}}}. \tag{25}$$

Assuming a 180 MVA DFIG (Table 4, appendix) and the operating points given in Fig. 2, the maximum arm currents amplitudes can be calculated using (16), considering (1)–(4) to calculate the rotor currents, (17) regarding the converter input side current, and (22)–(25) to determine the diagonal currents. The results for the operating points marked in Fig. 2 are displayed in Fig. 4. The rotor currents increase linearly with the slip magnitude for both over- and undersynchronous operation when delivering active power, as shown in Fig. 4(a). However, the rotor currents are higher for undersynchronous operation, as a higher stator power is required in undersynchronous operation to achieve the necessary active power in the grid [see (6)]. The diagonal currents show the specific amplitudes as specified in (22) and (23) for low-frequency operation. The results for pure reactive power with $\alpha = 0$ are shown in subfigure (b). It can be seen that the M3C output currents (rotor currents) are very low due to the low active power of the machine. The rotor currents only enable the magnetization of the machine. Thus, the entire converter current

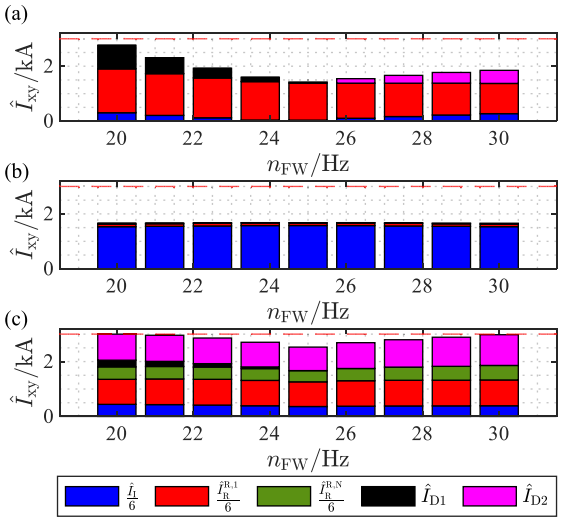

FIGURE 4. Composition of the maximum arm current at $\alpha = 0$, $k_T = 1.7$, and $N_P = 2$ for (a) $P_G = 290$ MW, $Q_G = 0$ Mvar, $U_G = U_{G,r}$. (b) $P_G = 0$ MW, $Q_G = 290$ Mvar, $U_G = U_{G,r}$. (c) $P_G = 0$ MW, $S_K = 290$ Mvar, $U_G = 0.1 \cdot U_{G,r}$.

carrying capacity can be used to provide reactive power at the input. Therefore, the M3C can be overloaded in reactive power operation, in comparison to the active power operation, without risking damage on the semiconductors. This is a unique feature of the M3C in this application.

Subfigure (c) shows the arm currents for a grid voltage dip by 90%. The high natural current component to demagnetize the machine necessitates large diagonal currents, as both presented compensation measures have to be applied. Therefore, the system capability to provide short-circuit currents is reduced drastically. In transient events, like an LVRT, additional asymmetries in arm capacitor voltages are possible which require further increased diagonal currents and cause a further reduced short-circuit current contribution.

3) SPECIFIC M3C FEATURES IN DFIG APPLICATIONS

The balancing of arm energies is a further important task for the M3C due to its modular structure [11].

Therefore, the arm energies are divided into four independent space vectors (vertical, horizontal diagonal 1, and diagonal 2) on the basis of the coordinate transformation shown in [10]. The mean values of the arm energy space vectors are balanced using four separate controllers. For operation at low output frequencies, as it is the case with the DFIG, input current and common mode voltage are applied to balance power in vertical direction [10]. Hence, the M3C always requires an input current in this application, even if the system is in idle operation. Therefore, a minimum reactive power of the M3C $Q_{I,min}$ is introduced. This is an important difference compared to state-of-the-art DFIGs operated with 2L-VSCs or 3L-VSCs, which are applied in wind energy or pump storage applications. As the reactive power at the PCC has to comply with the set point, $Q_{I,min}$ has to be compensated by the stator of the DFIG considering (7). Furthermore, for a

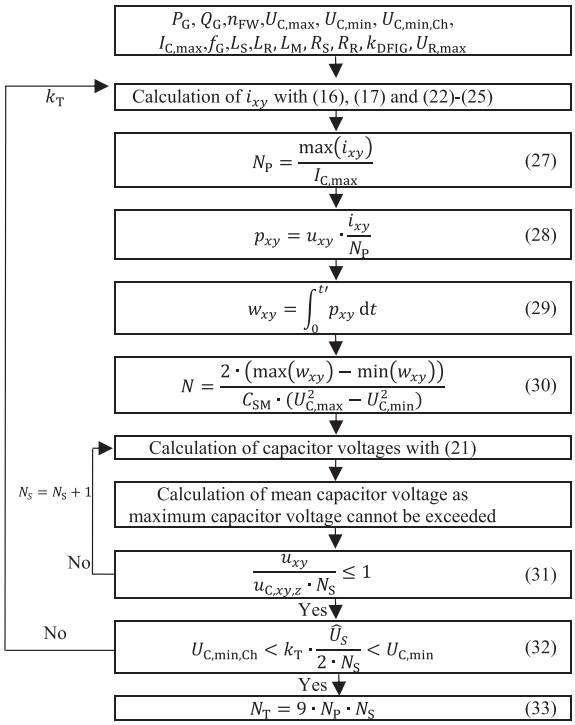

FIGURE 5. Design procedure for the modular multilevel matrix converter.

reactive power larger than $Q_{I,min}$, the distribution angle α is limited to

$$\alpha_{max} = 1 - \frac{Q_{I,min}}{Q_G}. \tag{26}$$

D. DESIGN OF THE M3C

The design of the M3C is done for a given submodule with specific IGBT modules and capacitances C_{SM}. Based on this constraint and the operating conditions, the required number of submodules can be derived using the scheme depicted in Fig. 5. In this article, the IGBT module *CM1500HC-90XA* from *Mitshubishi* is considered (4.5 kV, 1.5 kA). The module features a maximum pulsed collector current $I_{C,max}$ of 3 kA.

Alvarez et al. [12] proposed suitable boundaries for capacitor voltages of M2Cs (Fig. 6). It is useful to assume these boundaries also for the M3C. Therefore, the maximum capacitor voltage during normal operation $U_{C,max}$ corresponds to 64.4% of the rated IGBT blocking voltage, which gives 2.9 kV. The minimum capacitor voltage $U_{C,min}$ in normal operation is defined as 40% of the rated IGBT blocking voltage yielding 1.8 kV.

The energy to supply the electronics inside the cell, including gate drivers and measurements, is provided by the submodule capacitors. The energy supply requires a minimum capacitor voltage $U_{C,min,Ch}$ of 17.8% of the rated IGBT blocking voltage, which gives 800 V. To activate the submodules, this voltage must be surpassed during converter precharging from the grid. As the stator voltage is fixed by the machine, the transformer is used in order to satisfy this requirement (see (32)). The precharging voltage should also

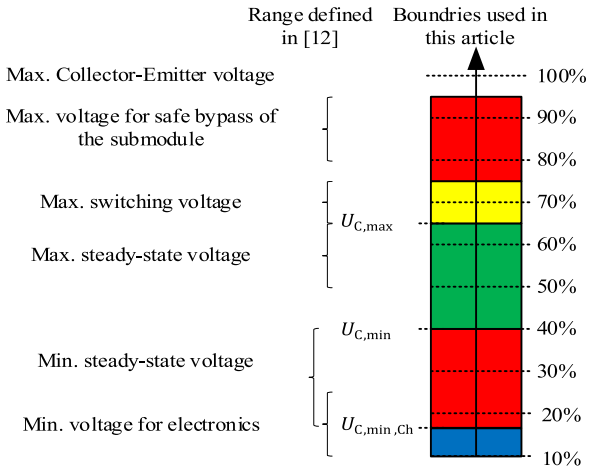

FIGURE 6. Submodule-capacitor voltage boundaries according to [12] depending on the rated IGBT module voltage class.

remain well under the minimum steady-state voltage. Taking the maximum pulsed collector current of the IGBT and the arm currents into account, the number of parallel arms can be calculated using (27) in Fig. 5. Based on the resulting arm power and energy [(28) and (29)], a minimum number of series-connected submodules can be estimated using (30).

To ensure that the mean capacitor voltages are the same in all operating points, it should be selected in such a way that the alternating parts [see (21)] do not exceed the voltage limits in the whole SOA in Fig. 2. Following that, one must verify if the necessary arm voltage can be synthesized across all operating points with the resulting capacitor voltages and the computed series connection number, as checked using (31). If this is not the case, N_S is increased. This iterative process is illustrated in Fig. 5.

The transfer ratio of the transformer determines the input voltage of the converter as well as the input current [see (17)], and therefore enables an optimization of the converter design. This optimization is achieved by the outer loop of the design procedure depicted in Fig. 5, minimizing the submodule count while considering the constraint outlined in (32). The total number of required full bridges can be calculated using (33).

The operating range (Fig. 2), the parameters of the DFIG, the submodule design (e.g., IGBT modules and capacitance), and the capacitor voltage constraints result to an M3C design with $N_S = 19$ and $N_P = 2$. Therefore, a total of 342 full-bridge modules are necessary with a mean capacitor voltage of 2460 V. The corresponding optimal transfer ratio of the transformer is 1.7.

III. LOSS CALCULATION

This section introduces a model of the total losses of the FESS, in order to derive the loss optimal reactive power distribution angle α in Section IV. At first, the losses of the DFIG are analyzed, while the second subsection focusses on the M3C. To the best of the author's knowledge, an analysis of the semiconductor losses of an M3C is not present in the literature.

A. DFIG

The dominating losses in the DFIG are identified as the friction losses $P_{L,FR}$, iron losses $P_{L,FE}$, as well as the ohmic losses $P_{L,DFIG,\Omega}$ in stator $\bar{P}_{L,S,\Omega}$ and rotor $\bar{P}_{L,R,\Omega}$

$$P_{L,DFIG} = \underbrace{\bar{P}_{L,S,\Omega} + \bar{P}_{L,R,\Omega}}_{P_{L,DFIG,\Omega}} + P_{L,FE} + P_{L,FR}. \tag{34}$$

The average ohmic losses of stator

$$\bar{P}_{L,S,\Omega} = 3 \cdot R_S \cdot \underbrace{\frac{1}{T} \cdot \int_0^T i_S^2 \cdot \mathrm{d}t}_{I_{S,rms}^2} \tag{35}$$

and rotor

$$\bar{P}_{L,R,\Omega} = 3 \cdot R_R \cdot \underbrace{\frac{1}{T} \cdot \int_0^T i_R^2 \cdot \mathrm{d}t}_{I_{R,rms}^2} \tag{36}$$

depend on the rms current and the corresponding resistance. The window length T is an integer multiple of the lowest time constant in the corresponding current. Both loss parts are influenced by the reactive power distribution of stator and rotor, as it influences the rotor and stator current. Equations (35) and (36) show the dependency of the ohmic machine losses on the rotor and stator currents. The presented analytical model of the machine in (1)–(13) can be used in order to calculate the currents dependent on the required reactive stator power.

In contrast, the iron losses $P_{L,FE}$ and friction losses $P_{L,FR}$ do not do not depend on the reactive power distribution α. As this article focusses on the M3C, these loss parts are not considered.

B. M3C

For M2Cs in high-power applications, the semiconductor losses mainly determine the overall losses. The resistive losses of the arm inductors, submodule capacitors, or the bus bars to connect the submodules are comparatively low [13]. The semiconductor losses can be divided into conduction and switching losses. When calculating the losses of a semiconductor, the switching state as well as the switching current and voltage have to be known. However, due to the used modulation method, the switching states cannot be predicted [11].

When examining a sufficiently long period of time T, each identical submodule performs the same switching actions on average, causing an equal loss distribution over all submodules [13]. The average conduction losses for one switch (diode or transistor) are calculated as follows [13]:

$$\bar{P}_{L,C,SC} = \frac{1}{T} \cdot \int_0^T d_{SC} \cdot i_{SC} \cdot u_{CE,sat}\left(i_{SC}, \vartheta_{SC}\right) \mathrm{d}t \tag{37}$$

with $SC \in \{1, 2, \ldots, 8\}$ accounting for the eight semiconducting devices within the full bridge. The parameter d_{SC} describes one of the duty cycles of the switches S1–S4 (see Fig. 3), i_{SC} the current through the corresponding semiconductor, $u_{CE,sat}$ the voltage drop over the semiconductor when

TABLE 1 Duty Cycles and Currents for the Conduction Loss Calculation

	S1		S2		S3		S4	
	D	T	D	T	D	T	D	T
SC	1	2	3	4	5	6	7	8
d_{SC}	d_{S1}	d_{S1}	d_{S2}	d_{S2}	d_{S3}	d_{S3}	d_{S4}	d_{S4}
i_{SC}	$i_{xy,\mathrm{p}}$	$i_{xy,\mathrm{n}}$	$i_{xy,\mathrm{n}}$	$i_{xy,\mathrm{p}}$	$i_{xy,\mathrm{n}}$	$i_{xy,\mathrm{p}}$	$i_{xy,\mathrm{n}}$	$i_{xy,\mathrm{p}}$

turned ON, and $\bar{\vartheta}_{SC}$ the mean temperature of the semiconductor.

The duty cycles d_{SC} are calculated using the duty cycle of the full bridge

$$d_{xyz} = \frac{u_{xy}}{N_{\mathrm{S}} \cdot u_{\mathrm{C},xy,z}}. \tag{38}$$

Considering the different switching states of the full bridge, the duty cycles of the switches can be specified [14]

$$d_{\mathrm{S1}} = \begin{cases} d_{xyz} & \text{if } d_{xyz} \geq 0 \\ 0 & \text{else} \end{cases} \tag{39}$$

$$d_{\mathrm{S2}} = d_{\mathrm{S3}} = \frac{1 - d_{\mathrm{S1}} - d_{\mathrm{S4}}}{2} \tag{40}$$

$$d_{\mathrm{S4}} = \begin{cases} |d_{xyz}| & \text{if } d_{xyz} < 0 \\ 0 & \text{else.} \end{cases} \tag{41}$$

Equations (37)–(41) show the dependency of the conduction losses of the semiconductors on the arm voltage and the arm capacitor voltage of the converter. The arm voltage can be calculated using (18), using the input voltage as well as the rotor voltage. For the calculation of the arm capacitor voltage, the arm energy is calculated according to (19)–(21). As the arm currents are a necessary value for this calculation, they are calculated according to (16), (17) and (22)–(25).

The current through the power electronic device i_{SC} depends on the arm current as well as the sign of the arm current since the IGBT only conducts the current from collector to the emitter. Reverse current will be conducted by the antiparallel diode. This has to be considered in the loss calculation, where

$$i_{xy,\mathrm{p}} = \begin{cases} |i_{xy}| & \text{if } i_{xy} \geq 0 \\ 0 & \text{else} \end{cases} \tag{42}$$

and

$$i_{xy,\mathrm{n}} = \begin{cases} |i_{xy}| & \text{if } i_{xy} < 0 \\ 0 & \text{else.} \end{cases} \tag{43}$$

These equations demonstrate the direct correlation between arm current and the losses of the M3C. Table 1 summarizes the duty cycles and switching currents for all diodes (D) and IGBTs (T) within the full bridge considering (38)–(43).

The average switching losses of the M3C are derived using an average switching frequency of $\bar{f}_{\mathrm{Sw}} = 125$ Hz, as well as the turn ON E_{on} and turn OFF Energy E_{off} of the semiconductor

$$\bar{P}_{\mathrm{L,S},SC} = \frac{\bar{f}_{\mathrm{Sw}}}{T} \cdot \int_0^T \left(E_{\mathrm{on}}\left(i_{SC}, u_{\mathrm{C},xy,z}, \bar{\vartheta}_{SC}\right) + E_{\mathrm{off}}\left(i_{SC}, u_{\mathrm{C},xy,z}, \bar{\vartheta}_{SC}\right)\right) \mathrm{d}t. \tag{44}$$

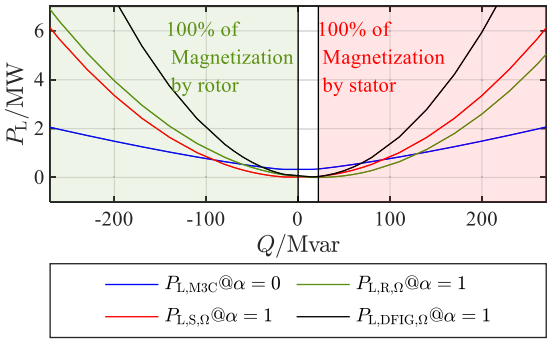

FIGURE 7. Losses of the M3C and DFIG at various reactive power levels, with a focus of the reactive power to the M3C or DFIG, individually. Also, an indication of the magnetization of the machine for $\alpha = 1$ is given.

The total losses of the M3C are derived using

$$\bar{P}_{\mathrm{L,M3C}} = N_{\mathrm{T}} \cdot \sum_{SC=1}^{8} \bar{P}_{\mathrm{L,S},SC} + \bar{P}_{\mathrm{L,C},SC}. \tag{45}$$

Equations (37) and (44) illustrate the evident dependency of the semiconductor losses on the arm current. The arm current, in turn, is contingent on the converter's power delivery and consumption [see (16) and (17)]. Consequently, next to the machine losses, the converter losses can also be influenced by the distribution of reactive power. An optimal distribution of the reactive power will be discussed in the following section.

IV. OPTIMUM REACTIVE POWER DISTRIBUTION

The following section derives the optimum distribution factor α_{opt} in order to reduce losses in the system, namely in converter and machine. This has not been done for the combination of M3C and DFIG. In order to use the model, frequencies and amplitudes of the currents and voltages under consideration must not change over a sufficiently long period of time T. Accordingly, a pure reactive power operation of the system is assumed, since the speed, and thus the rotor quantities of the machine change when applying active power. For the loss calculation, the parameters of the DFIG in Table 4 are used, as well as the converter design derived in Section II-D.

Equations (35)–(37) and (44) show that both the machine and the inverter losses depend on the respective currents as well as on the loss parameters of the DFIG ($R_{\mathrm{S}}, R_{\mathrm{R}}$) and the used IGBT and diode ($u_{\mathrm{CE,sat}}$, E_{on}, E_{off}).

In order to assess the magnitude of losses in the M3C as well as in the DFIG for specific reactive loads, Fig. 7 displays the DFIGs losses when delivering the entire reactive power through the stator, along with the inverter losses when delivering the entire reactive power through the M3C.

It can be observed that M3Cs losses are significantly lower at higher power levels compared to the DFIGs losses. This can be attributed, among other factors, to the smaller currents at the input of the M3C compared to the stator of the DFIG as they are stepped down through the transformer. Also, the losses never reach zero which is contributed to the minimum

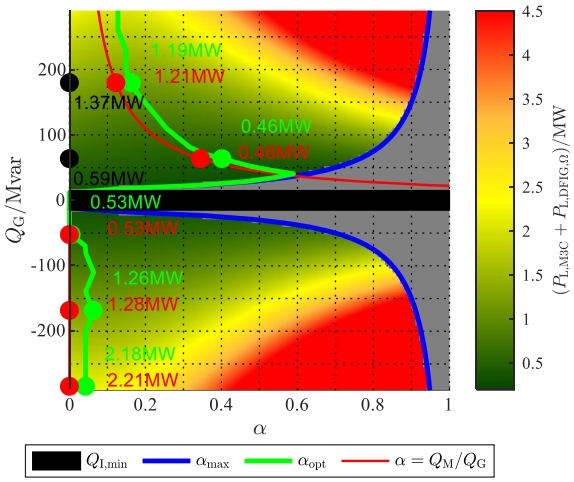

FIGURE 8. Losses of M3C and DFIG depending on reactive power and reactive power distribution factors, as well as the optimum power distribution.

input power of the M3C $Q_{\mathrm{I,min}} = 15$ Mvar, as well as the magnetization of the machine.

Furthermore, it is evident that the stator losses become zero at 0 Mvar. This is because the stator currents are zero [see (10)], consequently resulting in zero ohmic losses in the stator [see (35)]. However, the resistive losses of the rotor are not symmetrical around 0 Mvar. It is noticeable that the rotor losses become zero at approximately 22 Mvar. This phenomenon can be attributed to the magnetization of the machine, which is discussed in the following.

The machine requires a certain amount of reactive power for magnetization. This can be calculated using

$$Q_{\mathrm{M}} = \frac{U_{\mathrm{S}}^2}{\omega_{\mathrm{S}} \cdot L_{\mathrm{H}}} = 22.4\ \mathrm{Mvar} \tag{46}$$

neglecting the voltage drop across the stator resistance and stator leakage inductance.

This reactive power for magnetization can be applied through the stator, the rotor, or a combination of both. This is illustrated in Fig. 7. The required reactive power for magnetization of the given machine is 22.4 Mvar. Therefore, if the stator supplies a reactive power of 22.4 Mvar, the rotor currents will become zero, as the machine is entirely magnetized through the stator.

If the stator is required to deliver negative reactive power, the machine must be additionally magnetized through the rotor. This leads to higher rotor currents and results in higher losses compared to an equal magnitude of positive reactive power. Hence, in order to reduce losses, the machine should be magnetized over the stator for positive reactive powers.

With these insights, the results in Fig. 8 can be interpreted. The figure depicts the sum of α-dependent losses for different required reactive powers at the PCC, considering a specified distribution of the reactive power. Next to the losses, Fig. 8 also displays the blue boundary α_{max} resulting from (26). It assures a minimum reactive power at the input of the M3C to achieve an effective balancing (see Section II-C3).

To achieve the desired power in the grid, α should not exceed this blue line, and therefore remains outside the gray area. The black area indicates the minimum power of the M3C $Q_{\mathrm{I,min}} = 15$ Mvar. The remaining pairs of α and Q_{G} represent valid combinations. Therefore, α can be chosen freely in this area to generate minimum losses for a given reactive power, leading to an optimum reactive power distribution factor α_{opt} depicted in green. Considering the fact that the M3C causes significantly lower losses than the machine when delivering the same amount of reactive power (as shown in Fig. 7), it can be anticipated that the majority of the reactive power should be handled by the inverter. In addition, magnetization should occur through the stator for positive reactive power as discussed earlier. This would lead to an alpha value of

$$\alpha_{\mathrm{M}} = \frac{Q_{\mathrm{M}}}{Q_{\mathrm{G}}}. \tag{47}$$

for positive reactive power, as depicted in red in Fig. 8. This is corroborated by the green visualization of α_{opt} in Fig. 8. It can be observed that α_{opt} takes on very small values for negative reactive powers. For positive reactive powers, the majority of the magnetization power is supplied through the stator to minimize losses in the rotor. In addition, lower rotor currents contribute to reduced losses in the inverter, as the arm currents are decreased. Furthermore, the inverter does not need to provide an additional input power equal to the magnitude of the magnetization power, which additionally decreases the converter currents and therefore also the losses.

The deviation of the α_{opt} from the red curve can be attributed to the fact that the losses of an IGBT and the current through it have an approximately quadratic relationship (see Fig. 7). Hence, it can be reasonable to allocate a small portion of the power to the stator at high powers. This minor portion consequently results in lower power loss in the machine compared to the loss power that it would cause in the inverter as part of the larger power. However, the loss deviation between the red and green line are rather small (1%).

In contrast to supplying all reactive power over the converter (black bullet points in Fig. 8), up to 25% of power savings can be achieved by distributing the reactive power between the stator and the M3C. These significant power loss savings emphasize the importance of this newly introduced strategy.

V. EXPERIMENTAL VERIFICATION

A. TESTBENCH

To verify the findings of the article, the authors use a small-scale demonstrator. It consists of a 15-kVA M3C containing 108 full-bridge submodules equipped with the MOSFET *IPB156N22NFD*, and a 4-kW DFIG. The converter is controlled by a distributed control platform operating at 3 kHz [15]. Further parameters are listed in Table 2. All measurements are preformed using the analog–digital-converted values used by the control platform [15].

TABLE 2 Parameters of the Testbench

	Parameter	Value
M3C	Submodules per arm N_S	12
	Parallel arms N_P	1
	Maximum power	15 kvar
	Mean switching frequency $\overline{f}_{sw}$	250 Hz
	Mean capacitor voltage	90 V
DFIG	Stator resistance R_S	1.07 Ω
	Rotor resistance R'_R	1.32 Ω
	Stator inductance L_S	166.7 mH
	Rotor inductance L'_R	169.9 mH
	Magnetizing inductance L_M	160.1 mH
	Transfer ratio k_{DFIG}	400/950

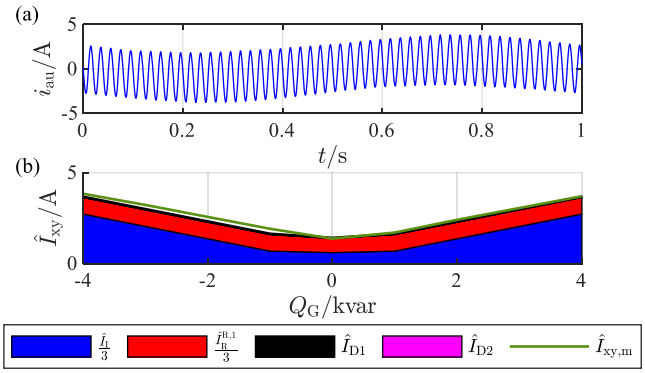

FIGURE 9. (a) Arm current for $Q_G = -4$ kvar, $P_G = 0.4$ kW, $n_{FW} = 1530$ rpm, $\alpha = 0$. (b) Arm current magnitude for $Q_G = -4 \ldots 4$ kvar, $P_G = 0.4$ kW, $n_{FW} = 1530$ rpm, $\alpha = 0$.

B. VERIFICATION OF THE DESIGN PROCESS

In this experiment, the arm currents were measured for various operating points. One out of the nine arm currents is depicted in Fig. 9(a) for the operating point at −4 kvar and $\alpha = 0$. It is showing the expected frequency superposition of grid, rotor, and diagonal frequencies. Furthermore, Fig. 9(b) shows the maximum arm current amplitude for various reactive powers. The results were recorded at rated DFIG speed of 1530 rpm.

The active power is determined by the losses of the system. The theoretically calculated values for each arm current component were compared with the measured amplitude $\hat{I}_{xy,m}$, revealing a very good agreement.

C. VERIFICATION OF THE PROPOSED LOSS MODEL

To verify the proposed analytical loss calculation of the M3C, the authors varied the reactive power distribution angle between 0 and 0.5 at a reactive power of −4 kvar. Therefore, the losses of the M3C can be analyzed at different reactive input powers of the M3C. With the subtraction of the measured active input power and rotor power, the losses of the M3C were derived. The results are depicted in Fig. 10. As the test bench is of much smaller power than the proposed high-power FESS, the loss distribution is different in comparison to a high-power application.

Beside to the semiconductor losses, the following losses have a significant influence:

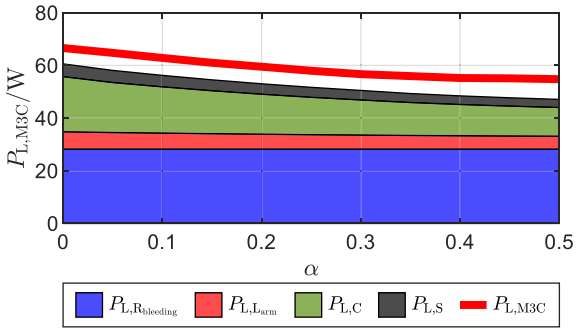

FIGURE 10. Loss measurement in the M3C of the test bench at $Q_G = -4$ kvar.

1) Losses of the bleeding resistors parallel to the submodule capacitors $P_{L,R_{bleeding}} = \frac{u_{C,xy,z}}{R_{bleeding}} \cdot N_T$.
2) Iron and ohmic losses in the arm inductors $P_{L,L_{arm}} = 9 \cdot R_{arm}(f) \cdot I_{xy}^2(f)$.

The parameters for the loss calculation are given in the appendix. Considering these additional losses of the system, an analytical loss calculation of the test bench is carried out. The comparison of the measurement and the analytical results are shown in Fig. 10. Measurement and analytical calculation agree well with minor discrepancies. These discrepancies can be attributed to parameter deviations of the components (MOSFETs, arm inductances, etc.), as well as measurement inaccuracies and thermal drifts.

D. VERIFICATION LOSS REDUCTION THROUGH REACTIVE POWER DISTRIBUTION

The authors calculated the optimum reactive power distribution for the test bench, as the loss parameters and power ranges differ significantly from the ones for the high-power system. It is depicted in the top plot of Fig. 11. It also matches the strategy suggested in (47). Also, the maximum α_{max} resulting from the minimum input power of 250 var is depicted. It can be seen that for negative reactive powers, α_{opt} is zero. The small discrepancy in contrast to the results of the high-power system in Fig. 8 can be attributed to higher losses of the machine in contrast to the converter, as the stator resistance of the machine is high compared to the low resistance MOSFETs in the M3C. It can be seen that for positive reactive powers, α_{opt} is as high as possible until the magnetizing power of the machine is reached (3.1 kvar). For higher positive reactive powers, α_{opt} drops, as the machine is then fully magnetized by the stator. Although the course of α_{opt} for the small-scale test bench exhibits the same characteristics as that of α_{opt} for the high-power system, the absolute values of α_{opt} differ due to the different power ranges and magnetization requirements of the machines.

The loss measurements in the bottom plot of Fig. 11 demonstrate a significant reduction in losses through the distribution of reactive power, as opposed to concentrating reactive power solely on the M3Cs input. The loss reduction is particularly noticeable for positive reactive power, as α deviates from

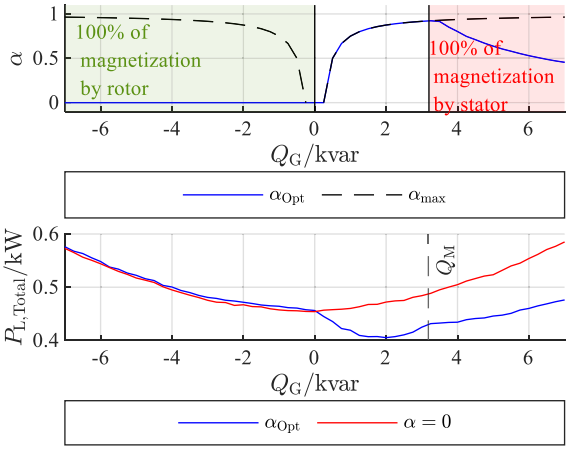

FIGURE 11. Top: optimum distribution of reactive power for power loss reduction, and indication of magnetization of machine. Bottom: losses of the system for different reactive powers in the grid and $\alpha = 0$ (red) and $\alpha = \alpha_{opt}$ (blue).

zero. A maximum loss reduction of 20% clearly indicates the significance of the proposed reactive power allocation. Therefore, the experimental results show a good agreement with the theoretical results in Fig. 8. The loss reduction is an important characteristic of the proposed FESS including M3C and DFIG.

VI. CONCLUSION

This article gives detailed insights in the function, design, and operating regime of the M3C in an FESS using a DFIG. A detailed design process for the converter is shown, considering the unique operating characteristics of the M3C in this application. A reactive power overload capability of the M3C, as well as the short-circuit current contribution of the system is shown. For the first time, an analytical-based loss calculation for an M3C is presented.

Using the model, an optimal distribution of reactive power between the stator and the matrix converter that minimizes losses and therefore operating costs is calculated. Experimental measurements on a low-power demonstrator were used to verify the analytical findings of this article.

APPENDIX

TABLE 3 Parameters for Loss Calculation in Test Bench

Parameter	Value
Bleeding Resistor $R_{bleeding}$	31 kΩ
Arm resistance R_{arm}@0Hz/@3kHz/@6kHz	96 mΩ/8 Ω/24 Ω

TABLE 4 Parameters of the DFIG

Parameter	Value
Stator resistance R_S	18 mΩ
Rotor resistance R'_R	16 mΩ
Stator inductance L_S	34 mH
Rotor inductance L'_R	34 mH
Magnetizing inductance L_M	32 mH
Number of pole pairs p	2
Stator voltage U_S	15 kV
Transfer ratio k	0.5

REFERENCES

[1] S. D'Arco and J. A. Suul, "Virtual synchronous machines—Classification of implementations and analysis of equivalence to droop controllers for microgrids," in *Proc. IEEE Grenoble Conf. PowerTech*, 2013, pp. 1–7.

[2] J. Kienast et al., "A new grid-stabilizing component: A flywheel energy storage system based on a doubly fed induction generator and modular multilevel matrix converter," in *Proc. 19th Int. Conf. AC DC Power Transmiss.*, 2023, pp. 246–253.

[3] Q. C. Zhong and G. Weiss, "Synchronverters: Inverters that mimic synchronous generators," *IEEE Trans. Ind. Electron.*, vol. 58, no. 4, pp. 1259–1267, Apr. 2011.

[4] A. Joseph and T. R. Chelliah, "A review of power electronic converters for variable speed pumped storage plants: Configurations, operational challenges, and future scopes," *IEEE J. Emerg. Sel. Topics Power Electron.*, vol. 6, no. 1, pp. 103–119, Mar. 2018.

[5] F. Kammerer, M. Gommeringer, J. Kolb, and M. Braun, "Benefits of operating doubly fed induction generators by modular multilevel matrix converters," in *Proc. PCIM Europe Conf. Proc.*, 2013, pp. 1149–1156.

[6] B. Rabelo and W. Hofmann, "Optimal active and reactive power control with the doubly-fed induction generator in the MW-class wind-turbines," in *Proc. Int. Conf. Power Electron. Drive Syst.*, 2001, pp. 53–58.

[7] A. Gensior, T. M. P. Nguyen, J. Rudolph, and H. Guldner, "Flatness-based loss optimization and control of a doubly fed induction generator system," *IEEE Trans. Control Syst. Technol.*, vol. 19, no. 6, pp. 1457–1466, Nov. 2011.

[8] G. Abad, J. Lopez, M. Rodriguez, and M. Luis, *Doubly Fed Induction Machine: Modeling and Control for Wind Energy Generation Applications*. Hoboken, NJ, USA: Wiley, 2011.

[9] J. Lopez, P. Sanchis, X. Roboam, and L. Marroyo, "Dynamic behavior of the doubly fed induction generator during three-phase voltage dips," *IEEE Trans. Energy Convers.*, vol. 22, no. 3, pp. 709–717, Sep. 2007.

[10] F. Kammerer, "System analysis and control of the modular multilevel matrix converter in drive applications (in German)," Dr. Hut, 2016, doi: 10.5445/IR/1000055761.

[11] F. Kammerer, J. Kolb, and M. Braun, "A novel cascaded vector control scheme for the modular multilevel matrix converter," in *Proc. IECON*, 2011, pp. 1097–1102.

[12] R. Alvarez, M. Wahle, H. Gambach, and J. Dorn, "Optimum semiconductor voltage level for MMC submodules in HVDC applications," in *Proc. 18th Eur. Conf. Power Electron. Appl.*, 2016, pp. 1–9.

[13] T. Modeer, H.-P. Nee, and S. Norrga, "Loss comparison of different submodule implementations for modular multilevel converters in HVDC applications," *EPE J.*, vol. 22, no. 3, pp. 32–38, Sep. 2012.

[14] V. Hofmann and M. M. Bakran, "Four-level MMC cell type with DC fault blocking capability for HVDC," in *Proc. PCIM Europe*, 2017, pp. 16–18.

[15] J. Kienast, A. Hoffman, M. Hoer, and S. Bernet, "Novel distributed control platform and algorithm for a modular multilevel matrix converter," *IEEE Trans. Power Electron.*, vol. 38, no. 7, pp. 8089–8101, Jul. 2023.